Topological Insulators for Thermoelectrics: A Perspective from Beneath the Surface

Michael Y. Toriyama[a*] and G. Jeffrey Snyder[a*]

Thermoelectric properties of topological insulators have traditionally been examined in the context of their metallic surface states. However, recent studies have begun to unveil intriguing thermoelectric effects emerging from bulk electronic states, which have largely been overlooked in the past. Charge transport phenomena through the bulk are especially important under typical operating conditions of thermoelectric devices, necessitating a comprehensive review of both surface and bulk transport in topological insulators. Here, we review thermoelectric properties that are uniquely observed in topological insulators, placing special emphasis on unconventional phenomena emerging from bulk states. We demonstrate that unusual thermoelectric effects arising from bulk states, such as band inversion-driven warping, can be discerned in experiments using a rather simple analysis of the weighted mobility. We believe that there is still plenty to uncover within the bulk, yet our current understanding can already inspire new strategies for designing and discovering topological insulators for next-generation thermoelectrics.

1 Introduction

Thermoelectric (TE) materials possess the unique ability to convert thermal energy to electrical energy and *vice versa*, allowing niche applications in energy conversion technologies across various domains. In generation mode (*i.e.*, heat to electricity), TE devices can be used to power remote devices such as deep-space probes [1] and Internet of Things sensors, [2] as well as to recover energy from waste heat. [3,4] Conversely, in Peltier cooling mode (*i.e.*, electricity to heat pumping), TE devices are used for targeted temperature control of optoelectronic and photonic devices [5,6] and serve as an eco-friendly alternative to refrigerants in traditional cooling systems. [7,8] The wide-ranging applications of TE technologies and can potentially address (i) the ever-growing societal demand for energy, particularly for cooling, [9] and (ii) global target of net-zero emissions by 2050. Achieving high TE power conversion efficiency is therefore critical for realizing such potential.

The efficiency of a TE device is critically dependent on the material used. The performance is determined by the material figure of merit $zT = S^2\sigma T/\kappa$, where S is the Seebeck coefficient, σ is the electrical conductivity, and κ is the thermal conductivity. These material properties are interconnected and often conflicting with one another (*e.g.*, increasing σ can also increase κ), making it challenging to optimize zT in a material. [10] Material engineering, and even material discovery, are therefore key areas for pushing the boundaries of TE technologies.

In the long history of TE research, numerous classes of materials have been examined. Topological insulators (TIs) are a relatively new class of materials that can be characterized as metal-like at the surface and semiconductor-like in the bulk. [11] In terms of the electronic structure, TIs possess gapless states at the surface while simultaneously having a band gap in the bulk. The unique properties of TIs make them promising for applications such as low-temperature spintronics. [12] At the same time, some

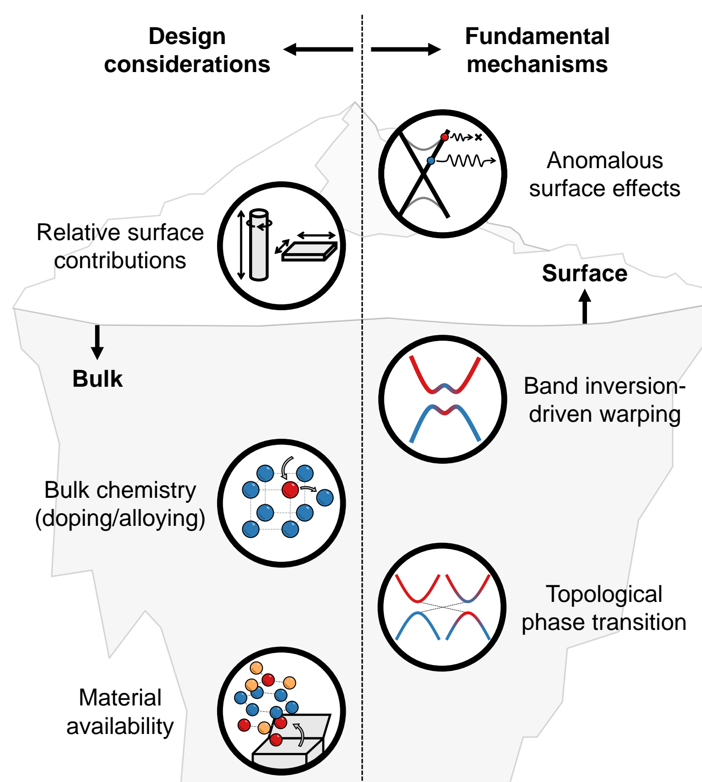

Figure 1 The "knowledge iceberg" of topological insulators in the context of thermoelectric properties and design. While surface states and emergent surface properties of topological insulators are well-known, there is much to uncover beneath the surface, pertaining to unique thermoelectric effects arising from bulk electronic states.

[a]Northwestern University, Evanston, IL 60208.
*E-mail: MichaelToriyama2024@u.northwestern.edu, jeff.snyder@northwestern.edu

https://doi.org/10.26434/chemrxiv-2024-zpmpp **ORCID:** https://orcid.org/0000-0002-2530-1390 Content not peer-reviewed by ChemRxiv. **License:** CC BY-NC 4.0

of the best TE materials today happen to be TIs, notably Bi_2Te_3-based materials. Because of this, in a rather *de facto* manner, many have speculated that TE power conversion is another encouraging application area for TIs.

With the recent surge in quantum materials research, many studies have begun to explore the exotic properties of TIs and their effects on TE properties.[13–17] After nearly a decade, the community has developed a strong fundamental understanding of atypical TE effects arising from TI surface states, such as geometric size dependencies and the anomalous Seebeck effect. Theoretical studies have suggested that the zT can be enhanced significantly by harnessing TI surface states; yet, theory is still leaps ahead of experimental realization in this aspect, partly due to conflicting requirements for synergizing both bulk and surface states to boost performance.

While many studies have focused on the effects of TI surface states on TE properties, comparatively less attention has been given to transport phenomena in the *bulk* of TIs. However, recent studies have shown that there are also unconventional TE effects arising from bulk electronic states in TIs, such as band inversion-driven warping and high valley degeneracy. We therefore view the current state of the cross-disciplinary field as a "knowledge iceberg" (Figure 1); quite literally, there are fascinating phenomena hidden *beneath the surface* of TIs that have become known only recently. Since the most widely-commercialized TE devices today are made of Bi_2Te_3-based TI alloys, a complete understanding of both surface *and* bulk transport properties of TIs is of practical importance for current, and future, TE technologies.

Unlike other reviews on the topic,[13–17] which nonetheless serve as valuable milestones in the field, we provide a comprehensive update on how surface *and* bulk properties unique to TIs affect TE transport properties. We begin with a self-contained overview of how TI surface states impact TE properties, drawing from over a decade of experimental and theoretical research. We then discuss practical considerations/strategies for enhancing zT in TIs, ideally by utilizing both surface and bulk transport channels convergently. At the core of this work, we review recent developments in understanding the bulk electronic structure and bulk charge transport properties of TIs. We demonstrate that unconventional phenomena stemming from bulk states, such as band inversion-driven warping, can be discerned in experiments by performing a rather simple analysis of the weighted mobility. We hope that this review encourages further in-depth research into the unique properties of TIs, especially those emerging from bulk states.

2 Topological surface states and thermoelectric properties

The prospect of using TIs for TE applications has historically been driven by the idea of leveraging TI surface states to boost zT.[13–17] The surge in TI research in recent years has resulted in a better understanding of exotic phenomena not normally observed in conventional (non-TI) materials. It is widely accepted now that TI surface states can strongly affect TE properties, in both constructive and detrimental ways. There are also important material considerations in leveraging surface-related effects in practical TE devices. Here, we summarize our current understanding of TE properties that emerge from TI surface states, and list several factors that influence the relative importance of surface states in charge transport phenomena.

2.1 Exotic phenomena

Charge transport properties are generally influenced by the electronic band structure of a material. In TIs, the band structure of the surface is characteristically different from that of the bulk, resulting in distinct transport behaviors through the two channels. It is therefore important to note the relative contributions from the surface and bulk, which will depend on the number of available states and hence the geometry of the sample (*i.e.*, surface area and bulk volume). The transport properties of interest here, namely the conductance (G) and Seebeck coefficient (S), can be expressed in terms of the individual transport channels as

$$G = G_b + G_s$$
$$S = \frac{S_b G_b + S_s G_s}{G_b + G_s}, \quad (1)$$

where the subscripts b and s denote the bulk and surface, respectively. Because both bulk and surface states contribute to

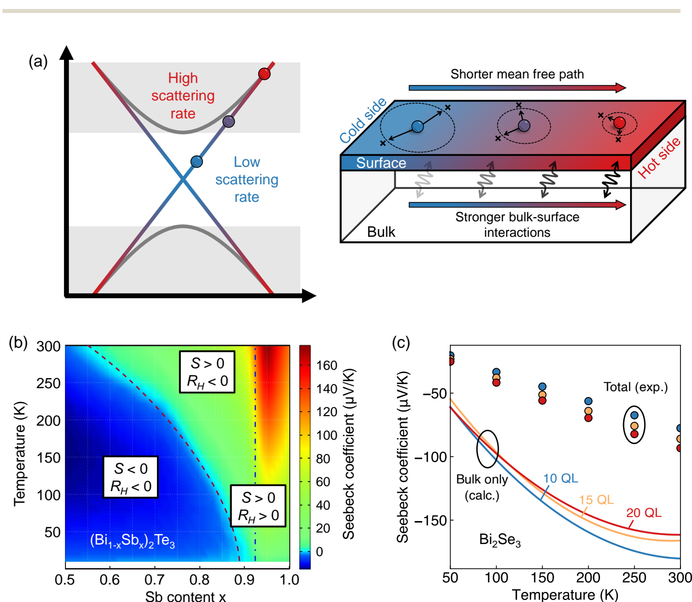

Figure 2 (a) Origin of the sign anomaly for carriers on the surface of a topological insulator. Surface carriers on the cold side have higher mean free path due to less backscattering than surface carriers on the hot side, which experience strong coupling with bulk states. (b) The anomaly is observed in thin films of $(Bi_{1-x}Sb_x)_2Te_3$, where a sign mismatch between the Seebeck coefficient (S) and Hall coefficient (R_H) is observed at some alloy compositions and temperatures. Figure adapted with permission from Ref. 18. (c) The Seebeck coefficient of thin films of Bi_2Se_3 consisting of 10, 15, and 20 quantum layers (QLs). The experimentally-measured values are plotted as points. Contributions from only the bulk states, which are calculated using a fitted transport model, are shown as lines. Data adapted with permission from Ref. 19.

https://doi.org/10.26434/chemrxiv-2024-zpmpp ORCID: https://orcid.org/0000-0002-2530-1390 Content not peer-reviewed by ChemRxiv. License: CC BY-NC 4.0

the overall (measurable) transport quantities, unusual TE effects have been observed in TIs.

2.1.1 Sign anomaly of the Seebeck coefficient

Both theoretical and experimental studies have demonstrated that the sign of S_s alone can be opposite to that of bulk carriers.[20,21] The effect is sometimes called the *anomalous Seebeck effect*. The underlying physics can be understood by considering the scattering behavior. Suppose we have an n-type material and the majority carriers are electrons. When subjected to a temperature gradient, high-energy electrons would normally diffuse from the hot side of the sample to the cold side, resulting in a negative voltage on the cold end and a negative S by convention. However, if the mean free path (l_p) of low-energy electrons on the cold side is longer than l_p of high-energy electrons on the hot side, then a net diffusion towards the hot side can occur. This is the case for surface carriers (Figure 2a): surface states within the bulk band gap are protected against backscattering and therefore have low scattering rates (*i.e.*, high l_p), whereas higher-energy surface states interact with bulk states and experience more scattering events (*i.e.*, low l_p). As a result, more low-energy surface electrons diffuse away from the cold end than high-energy electrons from the hot end, resulting in a net positive voltage on the cold end and a positive S in an n-type material. Although specific details of the surface bands, such as carrier velocity and density of states, add complexity to the transport physics, the explanation reveals the essential role of scattering on charge transport in a thermal gradient.

The sign anomaly of S_s has been substantiated by experimental measurements[18,19,22] following its initial prediction.[20,21] Normally, the Hall coefficient (R_H) and S have the same sign which reflects the majority carrier type: positive for holes, negative for electrons. However, in thin film samples of $(Bi_{1-x}Sb_x)_2Te_3$ consisting of 5 quantum layers (QLs), opposing signs were measured near $x = 0.9$ for a wide temperature range;[18] in particular, R_H was found to be negative indicating an n-type sample, yet the measured S was positive (Figure 2b). Given that their samples were thin films and that their measurements were supported by first-principles calculations, the authors concluded that the sign mismatch was due to TI surface states.[18]

Since S_b and S_s can have opposite signs, the magnitude of the total S can suffer (according to Eq. 1). Guo et al. observed this phenomenon while studying thin films of Bi_2Se_3 consisting of 7 to 20 QLs ($\sim$ 5 to 140 nm).[19] Using models fitted to their transport measurements, the authors extracted S_b and compared its value to the measured S. Indeed, the authors found that S_b was consistently larger in magnitude than the total S (Figure 2c),[19] suggesting that the surface states had a subtractive effect on S.

2.1.2 Surface gap opening

Gapless TI surface states can experience strong bipolar conduction effects, which are not ideal for S. Several authors have therefore studied ways to open a band gap in TI surface states and the corresponding effects on TE properties. Hybridization between states on opposite surfaces of a TI can open a band gap at the Dirac point,[23,25–28] as evidenced by ARPES measurements

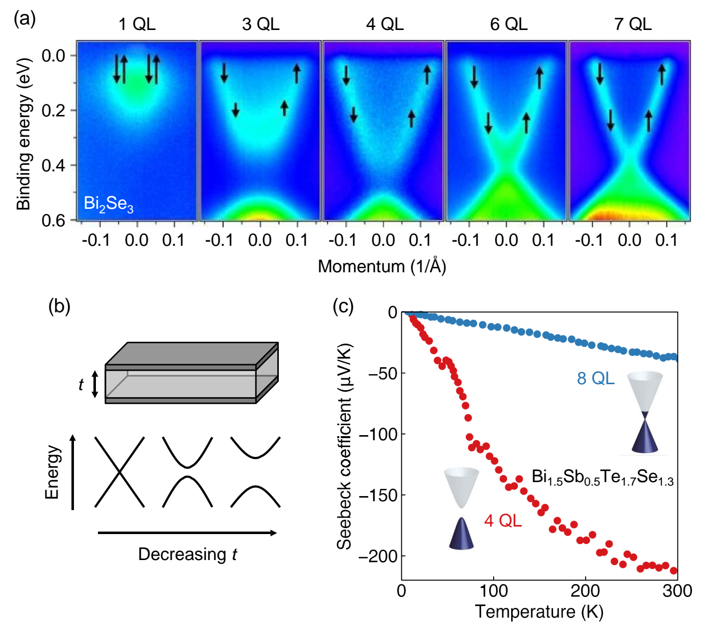

Figure 3 (a) ARPES measurements of Bi_2Se_3 thin films consisting of 1 – 7 quantum layers (QLs), where the arrows denote spin configurations of the surface states. Figure adapted with permission from Ref. 23. (b) Schematic of hybridization-induced gap opening in topological insulators. Electronic states on opposite surfaces experience stronger mixing as the film thickness (t) decreases, resulting in a gap opening/widening in surface bands. (c) Measured Seebeck coefficient on thin films of $Bi_{1.5}Sb_{0.5}Te_{1.7}Se_{1.3}$. A higher magnitude is observed in the thinner sample consisting of 4 QLs, indicating suppressed bipolar conduction effects and, as a result, gap opening. Data adapted with permission from Ref. 24.

on thin films of Bi_2Se_3 (Figure 3a).[23] With thinner samples and stronger wave function mixing, a band gap widening effect can be expected (Figure 3b). Theoretical studies have predicted that the zT can be enhanced due to the band gap opening, especially at low temperatures (< 150 K).[29–31] DFT calculations have shown that a surface gap opens in thin film Bi_2Te_3 when the film is composed of 1 or 2 QLs ($\sim$ 1 or 2 nm), and that the overall zT can be higher than in bulk samples.[32–34] Experimentally, a larger S was measured in a film of $Bi_{1.5}Sb_{0.5}Te_{1.7}Se_{1.3}$ consisting of 4 QLs (when a surface band gap opens) compared to a film of 8 QLs (when the gap closes),[24] suggesting that bipolar conduction effects are suppressed by a surface gap opening in thin film TIs (Figure 3c). External perturbations that break symmetry, such as strain and magnetic fields, can also result in a surface band gap opening and have been predicted to improve the power factor.[35]

2.2 Considerations for zT optimization

Arguably the most exciting question to ask when considering the use of TIs, as opposed to other types of materials, in TE devices is whether we can leverage TI surface states to boost zT. Theoretical predictions often demonstrate that zT can be enhanced by balancing charge transport along the surface with transport through the bulk (Figure 4a).[20,21,29–31,36] However, there are important factors that must be considered to utilize the surface and bulk channels synergistically.

https://doi.org/10.26434/chemrxiv-2024-zpmpp ORCID: https://orcid.org/0000-0002-2530-1390 Content not peer-reviewed by ChemRxiv. License: CC BY-NC 4.0

Table 1 Geometries of samples in which topological surface states are shown to influence thermoelectric properties.

Material	Sample type	Property	Value	Reference
$Bi_{0.9}Sb_{0.1}$	Film	Thickness	3 – 10 nm	40
Sb_2Te_3	Film	Thickness	32–160 nm	41
Bi_2Se_3	Nanowire	Height	71 – 124 nm	37
$Bi_{1.5}Sb_{0.5}Te_{1.7}Se_{1.3}$	Nanowire	Diameter	180 – 230 nm	42
$Bi_{1.5}Sb_{0.5}Te_{1.7}Se_{1.3}$	Film	Thickness	3 – 30 nm	22,24
$Bi_{1.1}Sb_{0.9}Te_2S$	Film	Thickness	3 – 113 μm	38

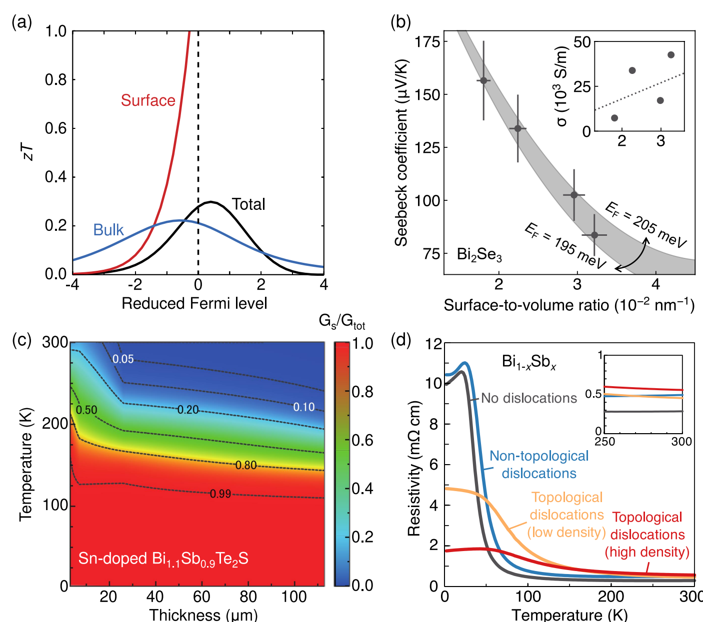

Figure 4 (a) Example breakdown of zT into the bulk and surface contributions. Figure adapted with permission from Ref. 20. (b) Seebeck coefficient and electrical conductivity (inset) for Bi_2Se_3 nanowires with varying surface-to-volume ratios. The shading represents a Fermi level range of 200 $\pm$ 5 meV. Figure adapted with permission from Ref. 37. (c) Ratio of surface conductance to the total conductance in films of Sn-doped $Bi_{1.1}Sb_{0.9}Te_2S$. Figure adapted with permission from Ref. 38. (d) Electrical resistivity of $Bi_{1-x}Sb_x$ with dislocations, either along slip systems that host topological surface states (*i.e.*, topological dislocations) or those that do not. Figure adapted with permission from Ref. 39.

2.2.1 Surface area

The degree to which surface states affect TE properties depends on the surface area of the sample compared to the bulk volume. TIs with greater surface area will be more strongly influenced by their surface states. Accordingly, geometric factors such as the material thickness, porosity, and grain size, as well as processing conditions that impact material geometry, become important considerations for TIs.[43–46]

It was demonstrated in nanowires of Bi_2Se_3 that increasing the surface-to-volume ratio leads to a corresponding decrease in S, despite an increase in σ (Figure 4b).[37] Here, the surface-to-volume ratio is used to quantify the relative contribution from surface states to transport, where samples with higher ratios experience stronger relative contributions. Although one may initially attribute the observed transport behavior to variations in the E_F position, further quantitative assessment with a two-channel transport model[36] suggested that E_F remained fairly constant for the measured samples (Figure 4b) and therefore could not explain the variations in transport properties. A monotonic decrease in the Seebeck coefficient was also observed in thinner films of Bi_2Se_3[19] and Sb_2Te_3,[41] both of which were attributed to the presence of TI surface states. A crossover in the temperature-dependent resistivity from bulk-dominated (semiconductor-like) to surface-dominated (metallic) behavior was observed in films of $Bi_{1-x}Sb_x$, when the thickness was reduced from 239 Å to 29 Å.[40]

The effects of TI surface states on TE properties are pronounced when the surface area of the sample is large compared to the bulk volume, meaning that the volume must be small. A natural question to ask then is: how small is "small enough"? Although the influence of surface states is dependent on the material, the sample dimension is typically smaller than 1 μm (Table 1), with the exception of $Bi_{1.1}Sb_{0.9}Te_2S$.[38] Stronger effects are observed in samples on the order of a few nm. Note that in studies of tetradymite compounds (*e.g.*, Bi_2Te_3) that report heavy influence from surface states, the sample geometry is typically expressed in terms of the number of QLs, where 1 QL is roughly 1 nm.

2.2.2 Temperature

The relative influence of surface states compared to bulk states is regulated by temperature through inelastic electron-phonon scattering[20] and Coulombic energy transfer.[47] Even near room temperature, enhanced phonon-assisted scattering between surface and bulk states was observed in Bi_2Se_3 through time- and angle-resolved photoemission spectroscopy.[48] The effects of surface states on TE properties are therefore more pronounced at lower temperatures, and the influence of surface states may become overwhelmed by bulk states at higher temperatures.

Theoretical calculations have shown that significant enhancements in zT can be achieved in thin films of Bi_2Te_3 below 150 K.[29] An experimental study on Sn-doped $Bi_{1.1}Sb_{0.9}Te_2S$ found that surface conduction dominates ($>$ 50%) over bulk conduction at temperatures below 200 K (Figure 4c).[38] In $Bi_{1-x}Sb_x$ TIs, two types of edge dislocations were introduced by plastically deforming the material along different compression axes: those that

https://doi.org/10.26434/chemrxiv-2024-zpmpp ORCID: https://orcid.org/0000-0002-2530-1390 Content not peer-reviewed by ChemRxiv. License: CC BY-NC 4.0

hosted surface states (*i.e.*, topological dislocations), and those that did not.[39] While the measured resistivity of samples with topological dislocations was markedly lower than those without topological dislocations below 50 K (Figure 4d), the resistivity was *higher* near room temperature (inset of Figure 4d). The low temperatures needed to access the potential benefits of TI surface states may limit their applicability in practical TE devices, which are typically deployed at or above room temperature.

2.2.3 Fermi level

One of the most important considerations for TEs in general is the Fermi level (E_F) position, which can be adjusted through chemical doping or, in some cases, gate tuning.[49–51] The E_F position strongly affects charge transport properties and, as a result, zT. In TIs, the E_F position is especially important because it modulates the relative contributions from bulk and surface states to TE properties. In fact, various transport models have shown that the zT, with contributions from both bulk and surface states, is optimized at a different E_F position than the zT from bulk states alone (Figure 4a).[20,30,31,36] As a result, a major challenge in optimizing the overall zT of TIs is to find E_F that balances bulk and surface transport.

It is also important to track the E_F position when attributing observed changes in TE properties to mechanisms related to TI surface states.[14,17] In particular, increasing the contributions from surface states by, *e.g.*, increasing the surface-to-volume ratio, has the same effects on TE properties as increasing the carrier concentration: both lead to an increase in σ and decrease in S. To avoid misattributing TE effects to surface states, it is essential to resolve the E_F position relative to the band edges and Dirac point.

One way to estimate the E_F position is by supplementing experimental measurements with transport modeling. Shin et al., for example, measured the properties of Bi_2Se_3 nanowires with varying surface-to-volume ratios and observed opposite trends between σ and S (Figure 4b),[37] which could be due to variations in the carrier concentration. By supporting their measurements with a two-channel transport model,[36] they demonstrated that E_F varies by no more than 10 meV in their samples (Figure 4b), providing strong evidence that size effects from surface states are the principal mechanism behind the reverse trends in σ and S, rather than being a carrier concentration effect. Hamdou et al. found using a similar two-channel model that the negative to positive transition in S with increasing Sb content in $(Bi_{1-x}Sb_x)_2Te_3$ nanowires can be explained by a shift in E_F relative to the Dirac point.[52] In this case, they dismissed potential effects from TI surface states, rather than attributing property trends to a variation in the surface-to-volume ratio.

The E_F position can also be estimated from magnetotransport measurements.[24,42,53] Hsiung et al., for example, found that synthesizing nanowires of $Bi_{1.5}Sb_{0.5}Te_{1.7}Se_{1.3}$ can boost the power factor by nearly an order of magnitude compared to bulk samples.[42] They concluded that the improvement is due to surface states by calculating the E_F position from the cyclotron mass and Fermi wave number, which they measured from the magnetoresistance and Shubnikov-de Haas oscillations.

3 Bulk properties in topological insulators for thermoelectrics

Topological insulators have generated widespread interest because of their protected surface states, often overshadowing investigations into their bulk properties. Yet, materials used in TE devices are typically on the scale of millimeters or larger, operate at room temperature or above, and are doped to carrier concentrations on the order of 10^{19} cm^{-3} and above, where the effects of surface states are less pronounced and potentially outweighed by bulk transport. Recent findings have revealed that unconventional transport phenomena can also emerge from bulk TI states, driven fundamentally by band inversion. In this section, we redirect our attention to bulk TE effects that are unique to TIs, opening up new opportunities to enhance zT in practical applications.

3.1 Phenomenological bulk effects unique to topological insulators

3.1.1 Band inversion-driven warping

One of the most important material properties for TEs is the valley degeneracy (*i.e.*, the number of carrier pockets that are contributing to charge transport in the bulk). Higher valley degeneracy improves the power factor, provided that intervalley scattering effects are not significant.[54,55] In TIs, the valley degeneracy is fundamentally linked to band inversion.[56] Assuming band inversion occurs at a k-point labeled k_0, strong coupling interactions at k_0 can offset the band edges from k_0, leading to the formation of multiple carrier pockets (Figure 5a).[56] We refer to this phenomenon as *band inversion-driven warping*; the term warping refers to the nonparabolic "W" ("M") shape adopted by the conduction (valence) band as opposed to the conventional "U" ("upside-down U") shape (Figure 5a).

Band warping, however, does not always occur in TIs simply due to band inversion. Recently, a $k \bullet p$ perturbation theory-based model was used to derive a mathematical condition for when inverted bands become warped in TIs that are centrosymmetric and obey time-reversal symmetry (*e.g.*, non-magnetic TIs).[56] Essentially, the bands must be sufficiently inverted for warping to occur; in other words, the *band inversion strength* of the TI must be large enough (Figure 5a). This is quantified by the leading-order parameter of the $k \bullet p$ model, M_0, defined as

$$|M_0| = \frac{E_{CB}(k_0) - E_{VB}(k_0)}{2}, \qquad (2)$$

where E_{CB} and E_{VB} are the conduction and valence band edges, respectively, and k_0 is the k-point where band inversion occurs. M_0 is the band inversion strength of a TI when the sign is negative, where more negative values correspond to stronger band inversion. Note that normal insulators with non-inverted bands can also be represented by a positive M_0. Because the band inversion strength is a characteristic of the electronic structure, it is principally modulated by (i) spin-orbit coupling (SOC)[57–59] and (ii) atomic orbital interactions (*e.g.*, sp-mixing).[60,61]

There are several examples of TIs that, despite being chemically similar, possess different valley degeneracies. A notable pairing is

https://doi.org/10.26434/chemrxiv-2024-zpmpp **ORCID:** https://orcid.org/0000-0002-2530-1390 Content not peer-reviewed by ChemRxiv. **License:** CC BY-NC 4.0

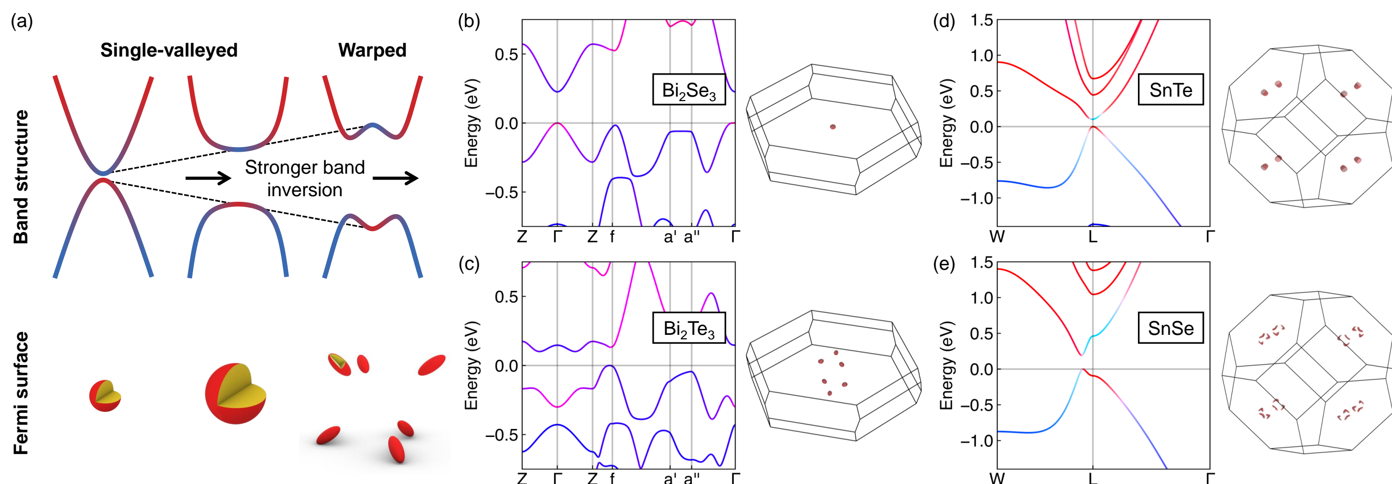

Figure 5 (a) Illustration of how the band structure and Fermi surface evolves with band inversion strength in a topological insulator. With stronger band inversion, the bands become warped, and the Fermi surface becomes multi-valleyed. The band structure and Fermi surface calculated using *ab initio* methods are shown for (b) Bi_2Se_3, (c) Bi_2Te_3, (d) SnTe, and (e) SnSe in the metastable rock-salt phase.

Bi_2Se_3 and Bi_2Te_3. While both TIs possess inverted bands at the Γ-point, the bands in Bi_2Se_3 are parabolic at the Γ-point resulting in a valley degeneracy of 1 (Figure 5b), whereas the bands are warped at the Γ-point in Bi_2Te_3 (Figure 5c). This suggests that the bands are sufficiently inverted at the Γ-point in Bi_2Te_3 but not in Bi_2Se_3. Indeed, the energy separation between the conduction and valence bands at the Γ-point is larger in Bi_2Te_3 (M_0 = -0.23 eV in Figure 5c) than in Bi_2Se_3 (M_0 = -0.12 eV in Figure 5b), which can be attributed to the stronger SOC in Bi_2Te_3. Due to the D_{3d} symmetry of the Γ-point, at least 2 carrier pockets can form from warped bands in Bi_2Te_3, though experimental measurements have indicated that the valley degeneracy can be greater than 6.[62]

In IV-VI rock-salt TIs, band inversion occurs at the L-point.[63] While the bands in SnTe are nearly parabolic and centered at the L-point with a valley degeneracy of 4 (Figure 5d), bands in the metastable rock-salt phase of SnSe are warped, giving rise to band edges that are offset from the L-point and a valley degeneracy of 24 (Figure 5e). The band inversion strength at the L-point is higher in SnSe (M_0 = -0.28 eV in Figure 5e) than in SnTe (M_0 = -0.05 eV in Figure 5d), providing further credence to the band inversion-driven warping phenomenon. In contrast to the tetradymite compounds, where the stronger SOC in Bi_2Te_3 leads to band warping, sp-mixing determines the band inversion strength in rock-salt compounds. Atomic orbital interactions can be affected by a number of factors, such as bond lengths and onsite orbital energies.[63]

3.1.2 Band warping and thermoelectric performance

In general, the benefits of high valley degeneracy on TE properties can be diminished by high scattering rates. Because band inversion-driven warping can lead to the formation of carrier pockets that are close in *k*-space, intervalley scattering by phonons (especially those near the zone center) may be significant. It is therefore natural to ask whether TE performance actually benefits from band warping in TIs.

In a recent study,[64] the effects of band inversion-driven warping on TE performance were studied. By considering a large set of materials using first-principles Boltzmann transport calculations, it was found that the maximum attainable zT (*i.e.* the zT value at the optimum doping level) tends to be higher for a TI than a conventional semiconductor, and even higher for TIs exhibiting stronger band inversion (Figure 6a). Further analysis showed that the high TE performance of TIs originates from a combination of low lattice thermal conductivity (κ_L) and high weighted mobility (μ_w) (Figure 6b). It is expected that TIs have low κ_L, because band inversion is typically induced by strong SOC interactions, which arises from the presence of heavy atoms. While the high-throughput calculations certainly confirm this, they also reveal that high μ_w is another key advantage of TIs over conventional semiconductors.

The results of charge transport modeling based on $k \bullet p$ perturbation theory were consistent with first-principles calculations.[64] Namely, the model showed that TIs exhibit high maximum zT that increases nearly monotonically with stronger band inversion strength (Figure 6c). The model also showed that the band inversion strength is a critical, if not the most important, material property that determines the maximum zT of a TI. As a result, band inversion-driven warping is the key advantage that TIs possess over conventional semiconductors for TE applications. Fundamentally, band warping in a TI gives rise to high μ_w (as revealed by first-principles calculations in Figure 6b) by reducing the conductivity mass and increasing the Seebeck mass (Figure 6d).

It is worth noting that increasing the band inversion strength improves the *maximum* zT of a TI, and the carrier concentration must still be optimized to achieve the maximum TE performance. It is therefore more precise to say that increasing the band inversion strength enhances the TE quality factor $B \propto \mu_w/\kappa_L$,[65] rather than the actual zT. Care must therefore be taken when attributing changes in TE properties to band inversion-related effects, especially when changes in the chemistry are involved (*e.g.*, doping and alloying). In such cases, both the band structure and the

https://doi.org/10.26434/chemrxiv-2024-zpmpp **ORCID:** https://orcid.org/0000-0002-2530-1390 Content not peer-reviewed by ChemRxiv. **License:** CC BY-NC 4.0

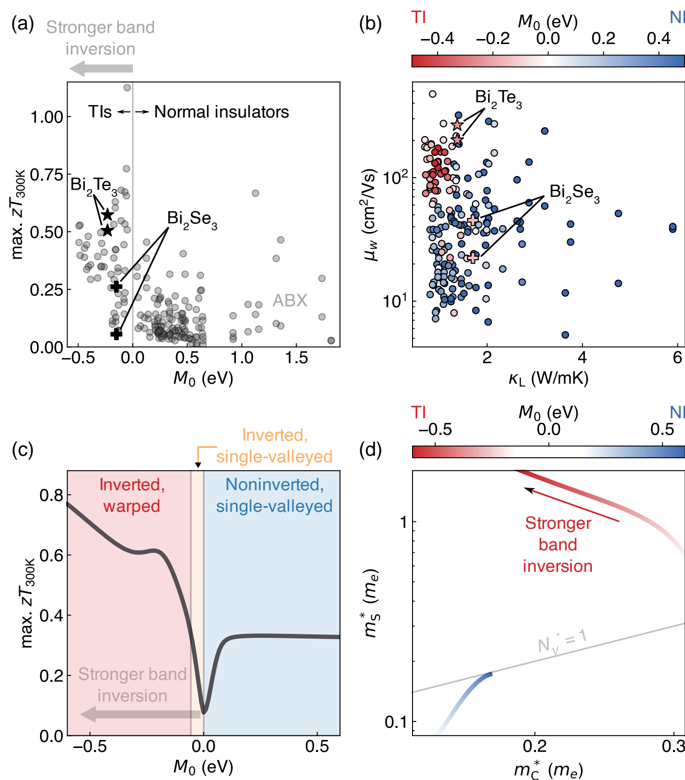

Figure 6 (a) Maximum attainable zT (optimized with respect to doping level) at room temperature, obtained using first-principles Boltzmann transport calculations. The maximum zT is plotted against the M_0 parameter (defined in Eq. 2) which, for topological insulators (TIs), represents the band inversion strength. (b) Weighted mobility (μ_w) and lattice thermal conductivity (κ_L), where TIs are represented by the red coloring (negative M_0) and normal insulators (NIs) are represented by the blue coloring. (c) Maximum attainable zT from charge transport modeling using $k \bullet p$ perturbation theory. The background coloring indicates the band structure shape (warped or single-valleyed) and topology (inverted or non-inverted). (d) Seebeck effective mass (m_S^*) and conductivity effective mass (m_C^*), where the red and blue coloring represent TIs and NIs, respectively. Figures adapted with permission from Ref. 64.

Fermi level are likely affected.

3.2 Strategies to improve bulk charge transport properties

Band inversion-driven warping can improve bulk TE properties in TIs and enhance the maximum attainable zT. Therefore, the TE performance can be improved directly by strengthening band inversion (*i.e.*, the degree to which the bands are inverted). The band inversion strength is determined principally by atomic orbital interactions and SOC interactions,[56] so strategies to manipulate band inversion in a TI should fundamentally aim to modulate these interaction strengths. We discuss some approaches in the following subsections.

A straightforward way to check whether band inversion-related phenomena are affecting TE properties in experiments is to check the weighted mobility (μ_w), which can be calculated directly from the electrical conductivity and Seebeck coefficient.[66] μ_w generally increases with the band inversion strength at a given temperature,[64] making it a strong indicator of warping effects in TIs. As we show in the following sections, analyzing μ_w allows us to provide compelling evidence that band inversion-driven effects are occurring in TIs.

3.2.1 Mechanical strain and external pressure

In general, applying external pressure or mechanical stress can modify the band structure of a material.[69,70] In TIs, strain can affect the band inversion strength by modulating nearest-neighbor orbital interactions.[71] In rock-salt IV-VI compounds, the energies of the L_6^- and L_6^+ bands (*i.e.*, those that are involved in band inversion, see Figure 7a) are influenced by sp-mixing between neighboring cations and anions.[63] Compression would enhance mixing between the cation-s and anion-p orbitals, which would raise the L_6^+ band relative to the L_6^- band and lead to stronger band inversion. First-principles calculations have shown that compressing SnTe leads to warping in the conduction band, splitting the conduction band edge into multiple valleys.[67] The n-type power factor was correspondingly three-fold larger than in the non-compressed state for a wide range of Fermi levels (Figure 7b), despite the scattering rates being nearly an order of magnitude higher.[67]

A similar behavior is observed in Bi_2Te_3-like TIs. First-principles calculations showed that compressing Bi_2Te_3, which correspondingly makes M_0 (defined in Eq. 2) more negative and thus increases the band inversion strength, improves the maxi-

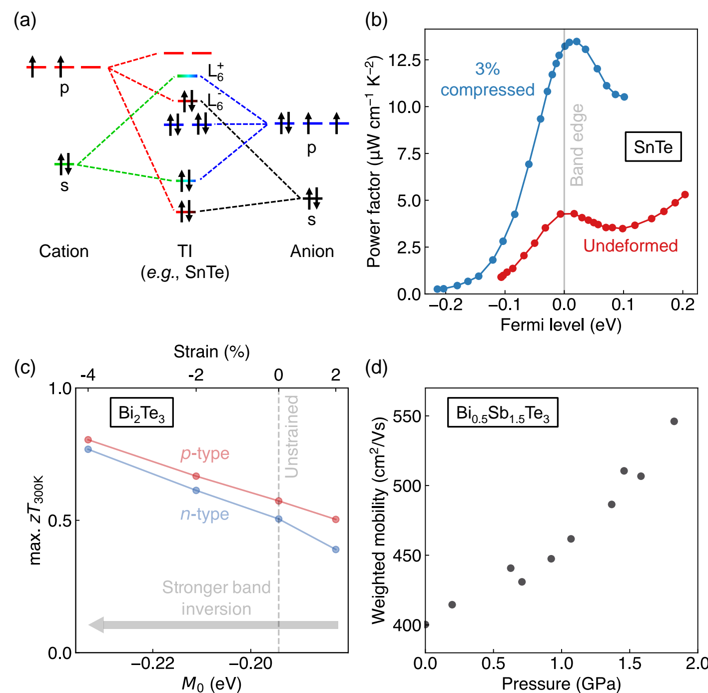

Figure 7 (a) Molecular orbital diagram for the L-point in IV-VI rock-salt phases, illustrating the inversion of the L_6^- and L_6^+ states. Figure adapted with permission from Ref. 63. (b) Calculated n-type power factor of undeformed and compressed SnTe. Data adapted with permission from Ref. 67. (c) Calculated maximum attainable zT of Bi_2Te_3 at different strain values, corresponding to varying degrees of band inversion strengths. Figure adapted with permission from Ref. 64. (d) Measured weighted mobility of $Bi_{0.5}Sb_{1.5}Te_3$ at different pressures. Data adapted with permission from Ref. 68.

https://doi.org/10.26434/chemrxiv-2024-zpmpp ORCID: https://orcid.org/0000-0002-2530-1390 Content not peer-reviewed by ChemRxiv. License: CC BY-NC 4.0

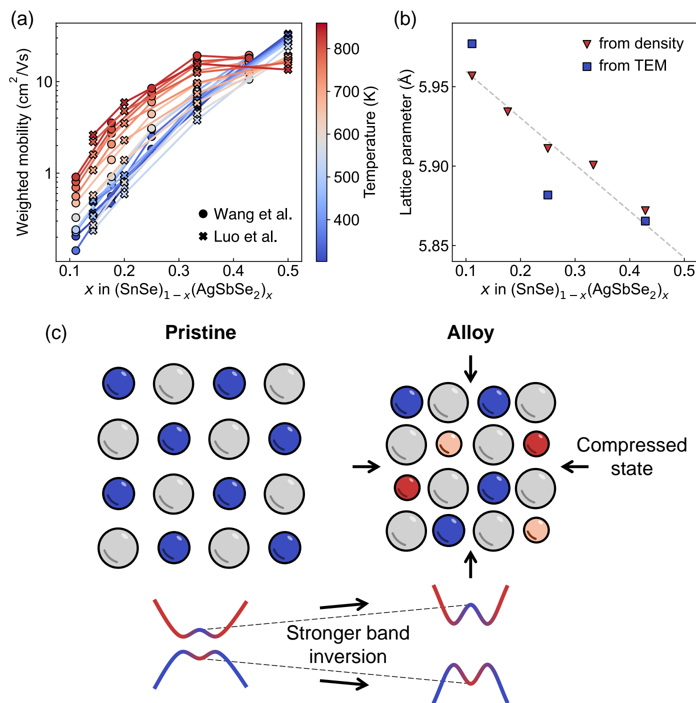

Figure 8 (a) Weighted mobility and (b) lattice constant of SnSe alloyed with $AgSbSe_2$. Data adapted with permission from Refs. 74 and 75. (c) Schematic of how alloying can affect the band inversion strength. Alloying-induced compression (*i.e.*, chemical pressure) leads to stronger band inversion in the parent topological insulator phase.

mum zT at room temperature for both n- and p-type (Figure 7c). Strain can be applied through external pressure, and improvements in the power factor with pressure have also been demonstrated experimentally.[68,72,73] We find from recent measurements of the TI $Bi_{0.5}Sb_{1.5}Te_3$[68] that μ_w increases with applied pressure (Figure 7d), which can be self-consistently explained as a band inversion-driven effect.

3.2.2 Alloying

Most TE materials are doped and/or alloyed to optimize zT. Since both techniques can affect the band structure and, as a result, the band inversion strength of a TI, transport properties can be regulated in unique ways by altering bulk chemistry. It has been suggested that even trace amounts of doping can affect TE properties, especially when the band structure is sensitive to small changes in SOC interactions.[57,58] However, phenomena resulting from band inversion are more readily observed in alloys rather than doped samples.

In particular, cubic alloys involving SnSe exhibit unconventional TE effects. The metastable rock-salt phase of SnSe is a known TI[76,77] with a highly warped band structure (Figure 5e),[63] and both theory[78,79] and experiments[80] have suggested capitalizing on its unique properties for TEs. Alloying SnSe with $AgSbSe_2$, for example, has been shown to improve the power factor across a wide range of temperatures.[74,75] A closer examination of the transport properties reveal that μ_w also increases with x in $(SnSe)_{1-x}(AgSbSe_2)_x$ (Figure 8a). Normally, μ_w of a two-phase mixture is lower than that of the end members, because the carrier mobility is lower. Wang et al. attributed the enhancement of μ_w to the compressive strain in rock-salt SnSe induced by $AgSbSe_2$ alloying, which is evidenced by the monotonic decrease in the lattice parameter determined from density and TEM measurements (Figure 8b).[74] Compressing rock-salt SnSe, which is a TI, strengthens sp-mixing and the band inversion strength in a manner similar to compressing SnTe (Section 3.2.1). Since rock-salt SnSe already has a warped band structure (Figure 5e), compression should further warp the band structure (Figure 8c), thus leading to higher μ_w. Presently, the increase in μ_w and power factor with the addition of $AgSbSe_2$ to SnSe has been substantiated on the basis of lattice compression and band inversion-related effects.[74] While the justification is certainly reasonable and self-consistent, in general, elemental substitution can also significantly modify the band inversion strength by modulating on-site energies.

Band inversion-related effects have been proposed in other alloy systems as well. Lattice compression and band gap widening were observed in $(PbSe)_{1-x}(ABX_2)_x$[81–83] similar to cubic alloys of SnSe, which can be explained as a gradual separation of the L_6^+ and L_6^- bands from stronger sp-mixing. First-principles calculations of an ordered supercell of $(PbSe)_{1-x}(AgSbS_2)_x$ ensured that the alloy undergoes a band inversion strengthening-type phenomenon primarily due to lattice compression, despite the chemistry being affected also by introducing Ag, Sb, and S.[83] Since pristine PbSe is a normal insulator, the observed band inversion-like effects indicate that PbSe likely undergoes a topological phase transition to a TI state upon alloying. In SnTe, the zT was boosted to nearly 1.4 after heavily alloying with GeTe and PbTe and doping with Cd.[84] Because first-principles calculations revealed that SnTe, upon alloying with GeTe and PbTe, adopts a multi-valleyed band structure, the improvement was attributed in large part to a band inversion-driven phenomenon.[84]

3.3 Topological phase transition

Alloys between a normal insulator, which has non-inverted bands, and a TI, which has inverted bands, allow us to understand how TE properties evolve through a topological transition from one band structure topology to another. Through this transition, the band gap closes at some critical composition x_c, where the bands become linear Dirac cones (Figure 9a).

There are several factors that affect x_c, such as temperature.[85–87] It is evident from optical measurements that increasing temperature shifts x_c towards a more Sn-rich composition in both $Pb_{1-x}Sn_xTe$ and $Pb_{1-x}Sn_xSe$, for example from $x_c \approx 0.4$ at 12 K to $x_c \approx 0.6$ at 300 K in $Pb_{1-x}Sn_xTe$ (Figure 9b). Fundamentally, changes in the topological transition behavior can be explained by orbital chemistry. In IV-VI rock-salt alloys, the transition involves an inversion of the L_6^+ and L_6^- bands (Figure 9a), which result from sp-mixing between the cation and anion (Figure 7a). Separating the cation and anion species by, *e.g.*, increasing temperature, would weaken sp-mixing, resulting in either a wider gap between the L_6^+ and L_6^- bands in a normal insulator or narrower gap in a TI (Figure 9c). In either case, x_c would shift towards the TI-rich side, explaining the increase in x_c with temperature in

https://doi.org/10.26434/chemrxiv-2024-zpmpp ORCID: https://orcid.org/0000-0002-2530-1390 Content not peer-reviewed by ChemRxiv. License: CC BY-NC 4.0

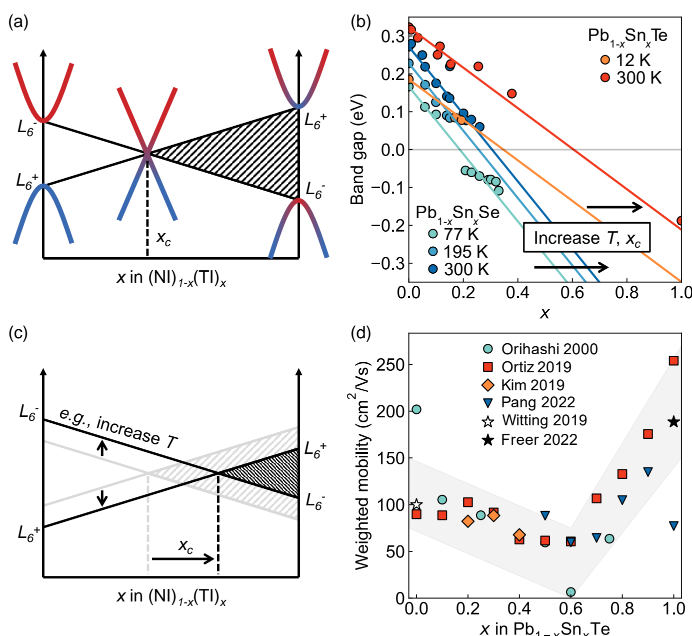

Figure 9 (a) Schematic of a topological transition in an alloy between a normal insulator (NI) and a topological insulator (TI). In alloys of IV-VI compounds, the transition occurs between the L_6^+ and L_6^- bands, where the band gap closes at composition x_c. (b) Band gap of $Pb_{1-x}Sn_xTe$ and $Pb_{1-x}Sn_xSe$, measured using optical techniques at different temperatures. By increasing the temperature (T), x_c also increases. Data adapted with permission from Refs. 85, 86, and 88. (c) Schematic of how external factors, such as temperature, can affect x_c by perturbing the L_6^+ and L_6^- bands. (d) Weighted mobility of $Pb_{1-x}Sn_xTe$ at room temperature. Data adapted with permission from Refs. 62,89–93.

$Pb_{1-x}Sn_xTe$ and $Pb_{1-x}Sn_xSe$ (Figure 9b).

The band structure evolution through the topological phase transition should influence TE properties. If the majority carrier type remains the same across the transition, then one may expect a minimum in the carrier effective mass and a maximum in mobility near x_c. Indeed, the effective mass has been shown to reach a minimum near x_c in $Pb_{1-x}Sn_xTe$.[94,95] However, there have been reports that appear to challenge expectations also.[90,96] Ortiz et al., for example, found that the room-temperature intrinsic mobility of undoped $Pb_{1-x}Sn_xTe$ reaches a maximum near $x \approx 0.3$,[90] as opposed to $x \approx 0.6$ where the topological transition is expected to occur (Figure 9a). Inconsistencies can arise because not all changes in properties are associated with changes in the band structure.

Interestingly, we find consistent agreement regarding one material property of undoped $Pb_{1-x}Sn_xTe$: the weighted mobility μ_w. By calculating μ_w from the measured electrical conductivity and Seebeck coefficient[66] across different studies,[89–92] we find that it reaches a minimum near $x \approx 0.6$ at room temperature (Figure 9d). Given that the alloy reaches a semimetallic state near this composition and semimetals typically exhibit low μ_w, it is reasonable to say that the minimal μ_w is attributable to the topological transition. Since the band structure evolution through the topological transition can be captured by a $k \bullet p$ band structure model,[97] modeling TE properties using an adapted transport model may help understand the origin of the weighted mobility trend.[98]

4 Outlook

The research landscape is now more fertile than ever for exploring topological insulators (TIs) for thermoelectric (TE) applications. Experimental and theoretical studies have jointly established a strong fundamental understanding of unconventional effects arising from TI surface states on TE properties. New discoveries of bulk transport phenomena in TIs, particularly those driven by band inversion, also create new opportunities for fundamental and technology-oriented research that extends underneath the widely-studied surface states. Bulk properties are especially important for practical applications such as Peltier coolers, which are typically on the scale of millimeters and operate near/above room temperature.

At the moment, there is limited attention to bulk states and corresponding bulk charge transport properties in TIs. While there are many materials that have been studied for TE[10,99] and TI[100,101] applications separately, there are only a handful that have been studied for both. The immediate impact of studying bulk TE properties is the expansion of the "material genome" at the relatively unexplored intersection of TIs and TEs. Valuable insight can be gained from material-agnostic transport models,[64] but concrete examples are needed to explore the complexities of real materials. Aside from the ones in this review, we believe that there are other known TI families where unconventional TE phenomena can be observed, such as $(SnSe)_{1-x}(ABX_2)_x$ alloys[102–108] and the homologous series of ternary $(TrCh)_n(Pn_2Ch_3)_m$ compounds, where Tr = tetrel (Ge, Sn, Pb), Pn = pnictogen (Sb, Bi), and Ch = chalcogen (Se, Te).[109–113] A more holistic understanding of band inversion-driven effects, complete with generalized models and case studies of specific materials, will enrich design strategies to improve zT in TI-based TEs. Since commercial Peltier cooling devices are typically composed of TI alloys ($Bi_2Te_{3-x}Se_x$ for the n-type leg and $Bi_{2-x}Sb_xTe_3$ for the p-type leg), better understanding of bulk TE properties unique to TIs also holds technological and economical significance.

There are also avenues for discovering new high-performing TE materials within the space of TIs. Many TIs, in fact, have been suggested as candidates for TEs, particularly half-Heuslers[114,115] and Zintl phases.[116] Past recommendations have often advertised the low lattice thermal conductivity stemming from the heavy atomic compositions of TIs, but exotic charge transport phenomena through the bulk can also fuel future TE discovery ventures. With the advent of computational methods to rapidly predict TE properties[117–121] combined with the availability of large-scale TI databases,[122,123] it is an opportune time for exploratory discovery of new TEs within known and predicted TIs. Even entirely new material classes that are yet to be explored by either the TI or TE communities can be investigated by coordinating high-throughput search workflows. We anticipate that data-driven approaches will guide future TE research and reveal an entirely new frontier for TI research rooted in TE applications.

Conflicts of Interests

There are no conflicts of interest to declare.

https://doi.org/10.26434/chemrxiv-2024-zpmpp ORCID: https://orcid.org/0000-0002-2530-1390 Content not peer-reviewed by ChemRxiv. License: CC BY-NC 4.0

Acknowledgements

M.Y.T. is funded by the United States Department of Energy through the Computational Science Graduate Fellowship (DOE CSGF) under grant number DE-SC0020347. M.Y.T. also acknowledges support from the Johannes and Julia Randall Weertman Graduate Fellowship. The authors acknowledge the support of award 70NANB19H005 from U.S. Department of Commerce, National Institute of Standards and Technology as part of the Center for Hierarchical Materials Design (CHiMaD).

References

1 T. C. Holgate, R. Bennett, T. Hammel, T. Caillat, S. Keyser and B. Sievers, *J. Electron. Mater.*, 2015, **44**, 1814.
2 M. Haras and T. Skotnicki, *Nano Energy*, 2018, **54**, 461.
3 T. Kuroki, K. Kabeya, K. Makino, T. Kajihara, H. Kaibe, H. Hachiuma, H. Matsuno and A. Fujibayashi, *J. Electron. Mater.*, 2014, **43**, 2405.
4 D. Ebling, A. Krumm, B. Pfeiffelmann, J. Gottschald, J. Bruchmann, A. C. Benim, M. Adam, R. Labs, R. Herbertz and A. Stunz, *J. Electron. Mater.*, 2016, **45**, 3433.
5 V. Semenyuk, Proceedings ICT2001. 20 International Conference on Thermoelectrics (Cat. No. 01TH8589), 2001, p. 391.
6 R. Enright, S. Lei, K. Nolan, I. Mathews, A. Shen, G. Levaufre, R. Frizzell, G.-H. Duan and D. Hernon, *Bell Labs Technical Journal*, 2014, **19**, 31.
7 L. E. Bell, *Science*, 2008, **321**, 1457.
8 G. J. Snyder, S. LeBlanc, D. Crane, H. Pangborn, C. E. Forest, A. Rattner, L. Borgsmiller and S. Priya, *Joule*, 2021, **5**, 748.
9 *The Future of Cooling*, https://www.iea.org/reports/the-future-of-cooling.
10 G. J. Snyder and E. S. Toberer, *Nat. Mater.*, 2008, **7**, 105.
11 M. Z. Hasan and C. L. Kane, *Rev. Mod. Phys.*, 2010, **82**, 3045.
12 K.-H. Jin, W. Jiang, G. Sethi and F. Liu, *Nanoscale*, 2023, **15**, 12787.
13 Y. Xu, *Chinese Phys. B*, 2016, **25**, 117309.
14 N. Xu, Y. Xu and J. Zhu, *npj Quant. Mater.*, 2017, **2**, 51.
15 J. Gooth, G. Schierning, C. Felser and K. Nielsch, *MRS Bull.*, 2018, **43**, 187.
16 C. Fu, Y. Sun and C. Felser, *APL Mater.*, 2020, **8**, 040913.
17 T. Yang, Y. Yang, X. Wang, G. Zhang and Z. Cheng, *Mater. Today Chem.*, 2023, **30**, 101488.
18 J. Zhang, X. Feng, Y. Xu, M. Guo, Z. Zhang, Y. Ou, Y. Feng, K. Li, H. Zhang, L. Wang, X. Chen, Z. Gan, S.-C. Zhang, K. He, X. Ma, Q.-K. Xue and Y. Wang, *Phys. Rev. B*, 2015, **91**, 075431.
19 M. Guo, Z. Wang, Y. Xu, H. Huang, Y. Zang, C. Liu, W. Duan, Z. Gan, S.-C. Zhang, K. He, X. Ma, Q. Xue and Y. Wang, *New J. Phys.*, 2016, **18**, 015008.
20 R. Takahashi and S. Murakami, *Phys. Rev. B*, 2010, **81**, 161302.
21 Y. Xu, Z. Gan and S.-C. Zhang, *Phys. Rev. Lett.*, 2014, **112**, 226801.
22 S. Y. Matsushita, K.-K. Huynh and K. Tanigaki, *Phys. Rev. B*, 2019, **99**, 195302.
23 M. Neupane, A. Richardella, J. Sánchez-Barriga, S. Xu, N. Alidoust, I. Belopolski, C. Liu, G. Bian, D. Zhang, D. Marchenko, A. Varykhalov, O. Rader, M. Leandersson, T. Balasubramanian, T.-R. Chang, H.-T. Jeng, S. Basak, H. Lin, A. Bansil, N. Samarth and M. Z. Hasan, *Nat. Commun.*, 2014, **5**, 3841.
24 S. Y. Matsushita, K. K. Huynh, H. Yoshino, N. H. Tu, Y. Tanabe and K. Tanigaki, *Phys. Rev. Mater.*, 2017, **1**, 054202.
25 J. Linder, T. Yokoyama and A. Sudbø, *Phys. Rev. B*, 2009, **80**, 205401.
26 C.-X. Liu, H. Zhang, B. Yan, X.-L. Qi, T. Frauenheim, X. Dai, Z. Fang and S.-C. Zhang, *Phys. Rev. B*, 2010, **81**, 041307.
27 H.-Z. Lu, W.-Y. Shan, W. Yao, Q. Niu and S.-Q. Shen, *Phys. Rev. B*, 2010, **81**, 115407.
28 Y. Zhang, K. He, C.-Z. Chang, C.-L. Song, L.-L. Wang, X. Chen, J.-F. Jia, Z. Fang, X. Dai, W.-Y. Shan, S.-Q. S. Shen, Q. Niu, X.-L. Qi, S.-C. Zhang, X.-C. Ma and Q.-K. Xue, *Nat. Phys.*, 2010, **6**, 584.
29 P. Ghaemi, R. S. Mong and J. E. Moore, *Phys. Rev. Lett.*, 2010, **105**, 166603.
30 R. Takahashi and S. Murakami, *Semicond. Sci. Tech.*, 2012, **27**, 124005.
31 H. Osterhage, J. Gooth, B. Hamdou, P. Gwozdz, R. Zierold and K. Nielsch, *Appl. Phys. Lett.*, 2014, **105**, 123117.
32 F. Zahid and R. Lake, *Appl. Phys. Lett.*, 2010, **97**, 212102.
33 J. Maassen and M. Lundstrom, *Appl. Phys. Lett.*, 2013, **102**, 093103.
34 J. Liang, L. Cheng, J. Zhang, H. Liu and Z. Zhang, *Nanoscale*, 2016, **8**, 8855.
35 M. Yarmohammadi and K. Mirabbaszadeh, *J. Mater. Chem. A*, 2019, **7**, 25573.
36 J. Gooth, J. G. Gluschke, R. Zierold, M. Leijnse, H. Linke and K. Nielsch, *Semicond. Sci. Tech.*, 2015, **30**, 015015.
37 H. S. Shin, B. Hamdou, H. Reith, H. Osterhage, J. Gooth, C. Damm, B. Rellinghaus, E. Pippel and K. Nielsch, *Nanoscale*, 2016, **8**, 13552.
38 S. Y. Matsushita, K. Ichimura, K. K. Huynh and K. Tanigaki, *Phys. Rev. Mater.*, 2021, **5**, 014205.
39 H. Hamasaki, Y. Tokumoto and K. Edagawa, *J. Phys. Soc. Jpn.*, 2020, **89**, 023703.
40 T. Hirahara, Y. Sakamoto, Y. Saisyu, H. Miyazaki, S. Kimura, T. Okuda, I. Matsuda, S. Murakami and S. Hasegawa, *Phys. Rev. B*, 2010, **81**, 165422.
41 N. F. Hinsche, S. Zastrow, J. Gooth, L. Pudewill, R. Zierold, F. Rittweger, T. Rauch, J. Henk, K. Nielsch and I. Mertig, *ACS Nano*, 2015, **9**, 4406.
42 T.-C. Hsiung, C.-Y. Mou, T.-K. Lee and Y.-Y. Chen, *Nanoscale*, 2015, **7**, 518.
43 O. A. Tretiakov, A. Abanov and J. Sinova, *Appl. Phys. Lett.*, 2011, **99**, 113110.
44 S. Izadi, J. W. Han, S. Salloum, U. Wolff, L. Schnatmann, A. Asaithambi, S. Matschy, H. Schlörb, H. Reith, N. Perez,

https://doi.org/10.26434/chemrxiv-2024-zpmpp **ORCID:** https://orcid.org/0000-0002-2530-1390 Content not peer-reviewed by ChemRxiv. **License:** CC BY-NC 4.0

K. Nielsch, S. Schulz, M. Mittendorff and G. Schierning, *Small*, 2021, **17**, 2103281.
45 S. Bayesteh, S. Sailler, H. Schloerb, R. He, G. Schierning, K. Nielsch and N. Perez, *Mater. Today Phys.*, 2022, **24**, 100669.
46 S. Izadi, A. Bhattacharya, S. Salloum, J. W. Han, L. Schnatmann, U. Wolff, N. Perez, G. Bendt, I. Ennen, A. Hütten, K. Nielsch, S. Schulz, M. Mittendorff and G. Schierning, *Small*, 2023, **19**, 2204850.
47 A. Principi and K.-J. Tielrooij, *Phys. Rev. B*, 2022, **106**, 115422.
48 Y. Wang, D. Hsieh, E. Sie, H. Steinberg, D. Gardner, Y. Lee, P. Jarillo-Herrero and N. Gedik, *Phys. Rev. Lett.*, 2012, **109**, 127401.
49 Y. Wang, F. Xiu, L. Cheng, L. He, M. Lang, J. Tang, X. Kou, X. Yu, X. Jiang, Z. Chen, J. Zou and K. L. Wang, *Nano Lett.*, 2012, **12**, 1170–1175.
50 D. Kim, P. Syers, N. P. Butch, J. Paglione and M. S. Fuhrer, *Nano Lett.*, 2014, **14**, 1701.
51 Y. Saito, T. Iizuka, T. Koretsune, R. Arita, S. Shimizu and Y. Iwasa, *Nano Lett.*, 2016, **16**, 4819.
52 B. Hamdou, J. Gooth, T. Böhnert, A. Dorn, L. Akinsinde, E. Pippel, R. Zierold and K. Nielsch, *Adv. Energ. Mater.*, 2015, **5**, 1500280.
53 J. Gooth, B. Hamdou, A. Dorn, R. Zierold and K. Nielsch, *Appl. Phys. Lett.*, 2014, **104**, 243115.
54 P. Norouzzadeh and D. Vashaee, *Sci. Rep.*, 2016, **6**, 22724.
55 J. Park, M. Dylla, Y. Xia, M. Wood, G. J. Snyder and A. Jain, *Nat. Commun.*, 2021, **12**, 3425.
56 M. Y. Toriyama and G. J. Snyder, *Cell Rep. Phys. Sci.*, 2023, **4**, 101392.
57 H. Shi, D. Parker, M.-H. Du and D. J. Singh, *Phys. Rev. Appl.*, 2015, **3**, 014004.
58 Devender, P. Gehring, A. Gaul, A. Hoyer, K. Vaklinova, R. J. Mehta, M. Burghard, T. Borca-Tasciuc, D. J. Singh, K. Kern and G. Ramanath, *Adv. Mater.*, 2016, **28**, 6436.
59 J. P. Heremans, R. J. Cava and N. Samarth, *Nat. Rev. Mater.*, 2017, **2**, 1.
60 Z. Zhu, Y. Cheng and U. Schwingenschlögl, *Phys. Rev. B*, 2012, **85**, 235401.
61 Z.-Y. Ye, H.-X. Deng, H.-Z. Wu, S.-S. Li, S.-H. Wei and J.-W. Luo, *npj Comput. Mater.*, 2015, **1**, 1.
62 I. T. Witting, T. C. Chasapis, F. Ricci, M. Peters, N. A. Heinz, G. Hautier and G. J. Snyder, *Adv. Electron. Mater.*, 2019, **5**, 1800904.
63 M. Y. Toriyama, M. K. Brod, L. C. Gomes, F. A. Bipasha, B. A. Assaf, E. Ertekin and G. J. Snyder, *J. Mater. Chem. A*, 2022, **10**, 1588.
64 M. Y. Toriyama and G. J. Snyder, *Mater. Horiz.*, 2024, **11**, 1188.
65 A. Zevalkink, D. M. Smiadak, J. L. Blackburn, A. J. Ferguson, M. L. Chabinyc, O. Delaire, J. Wang, K. Kovnir, J. Martin, L. T. Schelhas, T. D. Sparks, S. D. Kang, M. T. Dylla, G. J. Snyder, B. R. Ortiz and E. S. Toberer, *Appl. Phys. Rev.*, 2018, **5**, 021303.
66 G. J. Snyder, A. H. Snyder, M. Wood, R. Gurunathan, B. H. Snyder and C. Niu, *Adv. Mater.*, 2020, **32**, 2001537.
67 Y. Dai, W. Zhou, H.-J. Kim, Q. Song, X. Qian, T.-H. Liu and R. Yang, *npj Comput. Mater.*, 2022, **8**, 234.
68 F.-X. Bai, H. Yu, Y.-K. Peng, S. Li, L. Yin, G. Huang, L.-C. Chen, A. F. Goncharov, J.-H. Sui, F. Cao, J. Mao, Q. Zhang and X.-J. Chen, *Adv. Sci.*, 2022, **9**, 2105709.
69 S. V. Ovsyannikov and V. V. Shchennikov, *Chem. Mater.*, 2010, **22**, 635.
70 N. V. Morozova, I. V. Korobeinikov and S. V. Ovsyannikov, *J. Appl. Phys.*, 2019, **125**, 220901.
71 W. A. Harrison, *Pure Appl. Chem.*, 1989, **61**, 2161.
72 D. Polvani, J. Meng, N. Chandra Shekar, J. Sharp and J. Badding, *Chem. Mater.*, 2001, **13**, 2068.
73 I. Korobeinikov, N. Morozova, L. Lukyanova, O. Usov and S. Ovsyannikov, *Semiconductors*, 2019, **53**, 732.
74 H.-X. Wang, L.-S. Mao, X. Tan, G.-Q. Liu, J. Xu, H. Shao, H. Hu and J. Jiang, *Nano Energy*, 2018, **51**, 649.
75 Y. Luo, S. Hao, S. Cai, T. J. Slade, Z. Z. Luo, V. P. Dravid, C. Wolverton, Q. Yan and M. G. Kanatzidis, *J. Am. Chem. Soc.*, 2020, **142**, 15187.
76 Y. Sun, Z. Zhong, T. Shirakawa, C. Franchini, D. Li, Y. Li, S. Yunoki and X.-Q. Chen, *Phys. Rev. B*, 2013, **88**, 235122.
77 Z. Wang, J. Wang, Y. Zang, Q. Zhang, J.-A. Shi, T. Jiang, Y. Gong, C.-L. Song, S.-H. Ji, L.-L. Wang, L. Gu, K. He, W. Duan, X. Ma, X. Chen and Q.-K. Xue, *Adv. Mater.*, 2015, **27**, 4150.
78 D. Wang, W. He, C. Chang, G. Wang, J. Wang and L.-D. Zhao, *J. Mater. Chem. C*, 2018, **6**, 12016.
79 Y. Xie, Y. Zhou and X.-G. Gong, *Comp. Mater. Sci.*, 2018, **148**, 54.
80 G. Tang, Q. Wen, T. Yang, Y. Cao, W. Wei, Z. Wang, Z. Zhang and Y. Li, *RSC Adv.*, 2017, **7**, 8258.
81 S. Duan, H. Wang, G.-Q. Liu, Q. Wu, N. Man, Q. Zhang, X. Tan, Y. Yin, Y. Xiao, H. Hu, J. Xu, K. Guo, X. Yang and J. Jiang, *Nano Energy*, 2020, **78**, 105232.
82 J. Cai, J. Yang, G. Liu, L. Xu, X. Wang, H. Hu, X. Tan and J. Jiang, *Adv. Energ. Mater.*, 2022, **12**, 2103287.
83 J. Cai, R. Wang, S. Zhuang, F. Gao, M. Zhang, Z. Zhang, X. Tan, G. Liu and J. Jiang, *Adv. Funct. Mater.*, 2024, 2311217.
84 G. Xie, Z. Li, T. Luo, H. Bai, J. Sun, Y. Xiao, L.-D. Zhao, J. Wu, G. Tan and X. Tang, *Nano Energy*, 2020, **69**, 104395.
85 J. Dimmock, I. Melngailis and A. Strauss, *Phys. Rev. Lett.*, 1966, **16**, 1193.
86 A. Strauss, *Phys. Rev.*, 1967, **157**, 608.
87 B. M. Wojek, P. Dziawa, B. Kowalski, A. Szczerbakow, A. M. Black-Schaffer, M. Berntsen, T. Balasubramanian, T. Story and O. Tjernberg, *Phys. Rev. B*, 2014, **90**, 161202.
88 C.-F. Wu, T.-R. Wei and J.-F. Li, *Phys. Chem. Chem. Phys.*, 2015, **17**, 13006.
89 M. Orihashi, Y. Noda, L.-D. Chen, T. Goto and T. Hirai, *J. Phys. Chem. Solids*, 2000, **61**, 919.

https://doi.org/10.26434/chemrxiv-2024-zpmpp ORCID: https://orcid.org/0000-0002-2530-1390 Content not peer-reviewed by ChemRxiv. License: CC BY-NC 4.0

90 B. R. Ortiz, J. M. Adamczyk, K. Gordiz, T. Braden and E. S. Toberer, *Mol. Syst. Des. Eng.*, 2019, **4**, 407.

91 G. Kim, J. H. Yun and J.-S. Rhyee, *J. Phys. Chem. Solids*, 2019, **126**, 11.

92 H. Pang, X. Zhang, D. Wang, R. Huang, Z. Yang, X. Zhang, Y. Qiu and L.-D. Zhao, *J. Materiomics*, 2022, **8**, 184.

93 R. Freer, D. Ekren, T. Ghosh, K. Biswas, P. Qiu, S. Wan, L. Chen, S. Han, C. Fu, T. Zhu, A. K. M. A. Shawon, A. Zevalkink, K. Imasato, G. J. Snyder, M. Ozen, K. Saglik, U. Aydemir, R. Cardoso-Gil, E. Svanidze, R. Funahashi, A. V. Powell, S. Mukherjee, S. Tippireddy, P. Vaqueiro, F. Gascoin, T. Kyratsi, P. Sauerschnig and T. Mori, *J. Phys. Energy*, 2022, **4**, 022002.

94 J. Butler, *Solid State Commun.*, 1969, **7**, 909.

95 V. Jovovic, S. Thiagarajan, J. Heremans, T. Komissarova, D. Khokhlov and A. Nicorici, *J. Appl. Phys.*, 2008, **103**, 053710.

96 E. Rogacheva, G. Nikolaenko and O. Nashchekina, *J. Phys. Chem. Solids*, 2023, 111635.

97 A. Dmitriev, G. Lashkarev, V. Orletskii and K. Tovstyuk, *Phys. Status Solidi*, 1986, **135**, 587.

98 R. Gurunathan, S. Sarker, C. K. Borg, J. Saal, L. Ward, A. Mehta and G. J. Snyder, *Adv. Electron. Mater.*, 2022, **8**, 2200327.

99 J. Mao, G. Chen and Z. Ren, *Nat. Mater.*, 2021, **20**, 454.

100 W. Feng and Y. Yao, *Sci. China Phys. Mech.*, 2012, **55**, 2199.

101 Y. Ando, *J. Phys. Soc. Jpn.*, 2013, **82**, 102001.

102 H. Wang, H. Hu, N. Man, C. Xiong, Y. Xiao, X. Tan, G. Liu and J. Jiang, *Mater. Today Phys.*, 2021, **16**, 100298.

103 Y. Wang, B. Qin, T. Hong, L. Su, X. Gao, D. Wang and L.-D. Zhao, *Acta Mater.*, 2022, **227**, 117681.

104 S. Chandra, R. Arora, U. V. Waghmare and K. Biswas, *Chem. Sci.*, 2021, **12**, 13074.

105 H. Jang, M. Y. Toriyama, S. Abbey, B. Frimpong, J. P. Male, G. J. Snyder, Y. S. Jung and M.-W. Oh, *Adv. Mater.*, 2022, **34**, 2204132.

106 H. Jang, Y. S. Jung and M.-W. Oh, *Heliyon*, 2023, **9**, e21117.

107 J. Zhu, L. Bo, J. Kong, Y. Hou, L. Zhao, C. Li and D. Zhao, *J. Alloy. Compd.*, 2024, **971**, 172754.

108 Y. Wang, B. Qin, H. Shi, L. Su, D. Wang and L.-D. Zhao, *Acta Mater.*, 2023, **247**, 118754.

109 S. V. Eremeev, G. Landolt, T. V. Menshchikova, B. Slomski, Y. M. Koroteev, Z. S. Aliev, M. B. Babanly, J. Henk, A. Ernst, L. Patthey, A. Eich, A. A. Khajetoorians, J. Hagemeister, O. Pietzsch, J. Wiebe, R. Wiesendanger, P. M. Echenique, S. S. Tsirkin, I. R. Amiraslanov, J. H. Dil and E. V. Chulkov, *Nat. Commun.*, 2012, **3**, 635.

110 J.-Y. Tak, Y. S. Lim, J. N. Kim, C. Lee, J. H. Shim, H. K. Cho, C.-H. Park and W.-S. Seo, *J. Alloy. Compd.*, 2017, **690**, 966.

111 H. Wu, X. Lu, G. Wang, K. Peng, B. Zhang, Y. Chen, X. Gong, X. Tang, X. Zhang, Z. Feng, G. Han, Y. Zhang and X. Zhou, *Nano Energy*, 2020, **76**, 105084.

112 S. K. Kihoi, U. S. Shenoy, J. N. Kahiu, H. Kim, D. K. Bhat and H. S. Lee, *ACS Appl. Electron. Mater.*, 2023, **5**, 4504.

113 X. Qian, H. Jin, X. Li, B. Ding, J. Wang and S.-F. Wang, *Appl. Phys. Lett.*, 2024, **124**, 103902.

114 L. Müchler, F. Casper, B. Yan, S. Chadov and C. Felser, *Phys. Status Solidi*, 2013, **7**, 91.

115 J. Yang, *Materials Aspect of Thermoelectricity*, CRC Press, 2016, p. 597.

116 M. O. Ogunbunmi and S. Bobev, *J. Mater. Chem. C*, 2023, **11**, 8337.

117 J. Yan, P. Gorai, B. Ortiz, S. Miller, S. A. Barnett, T. Mason, V. Stevanović and E. S. Toberer, *Energ. Environ. Sci.*, 2015, **8**, 983.

118 G. Xing, J. Sun, Y. Li, X. Fan, W. Zheng and D. J. Singh, *Phys. Rev. Mater.*, 2017, **1**, 065405.

119 G. K. Madsen, J. Carrete and M. J. Verstraete, *Comput. Phys. Commun.*, 2018, **231**, 140.

120 A. M. Ganose, J. Park, A. Faghaninia, R. Woods-Robinson, K. A. Persson and A. Jain, *Nat. Commun.*, 2021, **12**, 2222.

121 M. Y. Toriyama, A. N. Carranco, G. J. Snyder and P. Gorai, *Mater. Horiz.*, 2023, **10**, 4256.

122 https://topologicalquantumchemistry.org.

123 Autes, Gabriel, Wu, QuanSheng, Mounet, Nicolas and Yazyev, Oleg V., *TopoMat: a database of high-throughput first-principles calculations of topological materials*, 2019, https://archive.materialscloud.org/record/2019.0019/v2.

https://doi.org/10.26434/chemrxiv-2024-zpmpp **ORCID:** https://orcid.org/0000-0002-2530-1390 Content not peer-reviewed by ChemRxiv. **License:** CC BY-NC 4.0